J. Phys.: Condens. Matter **9** (1997) 4437–4453. Printed in the UK PII: S0953-8984(97)79715-7

Harmonic flux penetration of superconductors in low-frequency, high-amplitude, alternating-current magnetic fields

H D Ramsbottom and D P Hampshire
Department of Physics, University of Durham, Durham, UK

Received 20 November 1996

Abstract. A critical-state model has been used to calculate the magnetic response of a superconducting sample to an applied a.c. magnetic field. The analysis has been performed for both a cylindrical and a slab geometry and evaluated up to the tenth harmonic. It is shown that standard expressions derived using the critical-state model which relate the critical current density to the d.c. magnetic moment can be used in a.c. measurements to within an accuracy of ~4% by replacing the term for the d.c. magnetic moment by $\sqrt{2}m_{rms}$(min), where m_{rms}(min) is the minimum lossless rms magnetic moment; the apparent penetration of the field beyond the centre of the sample (i.e. an overshoot) found in flux penetration measurements is an artifact of the analysis and cannot be used as direct evidence for granularity. Flux penetration measurements on non-granular NbTi from 4.2 K up to T_c in magnetic fields up to 10 T are presented which provide good agreement with calculations.

1. Introduction

Flux penetration measurements, developed by Campbell [1], provide a unique opportunity to study both the functional form and spatial variation of the critical current density (J_c) of superconductors, non-destructively. Such information has become increasingly important with the discovery of the high-temperature superconductors, where uniform J_c in such short-coherence-length materials is difficult to achieve. Flux penetration measurements make it possible to quantify the inhomogeneous properties of superconducting materials and locate regions of interest.

A number of authors have considered the low-field response of superconductors either for a.c. susceptibility measurements or flux penetration measurements [2–4]. They have shown that a strong field dependence for J_c (which can occur in strongly granular materials or materials with very weak pinning) can explain the non-physical results found in flux penetration measurements, namely that over a small range of a.c. magnetic fields, flux apparently penetrates beyond the centre of the sample (i.e. an overshoot occurs). However this effect has also been observed in high d.c. magnetic fields, where a strongly field-dependent J_c cannot explain the overshoot. This work shows that an overshoot inevitably follows from a uniform field-independent J_c. Results for a NbTi alloy which is considered to be a non-granular are presented, and good agreement with the analysis confirmed.

In section 2, the response of a superconducting sample to low-frequency, a.c. fields is calculated. Following Bean's work [5] the solution is given for low a.c. fields, i.e. for fields less than those required to fully penetrate the sample. The section also contains the

solutions for large a.c. fields, i.e. for fields greater than those required to fully penetrate the sample. A Fourier analysis is then used to generate the harmonic response of both the loss and lossless components for the first ten harmonics, i.e. from $1F$ to $10F$. Solutions are given for both a cylindrical and a slab geometry. Results are plotted graphically and values useful for analysing experimental data tabulated. Section 3 describes the NbTi sample measured and highlights experimental details. The sample is made from a commercial, multifilamentary, superconducting wire. It has been chosen because it is one of the most extensively characterized superconducting materials and can be assumed to be non-granular. Results are presented from 4.2 K up to T_c in magnetic fields up to 10 T. The analysis of the experimental data is shown in section 4. The results have been used to determine magnetic field profiles and the critical current density as a function of field and temperature. The magnetically measured $J_c(B, T)$ values are compared with transport current data on the same sample. Section 5 describes the harmonic response of the sample up to the tenth harmonic, $10F$. The results are compared with the theoretical predictions outlined in section 2. At the end of the paper, the most important findings are summarized.

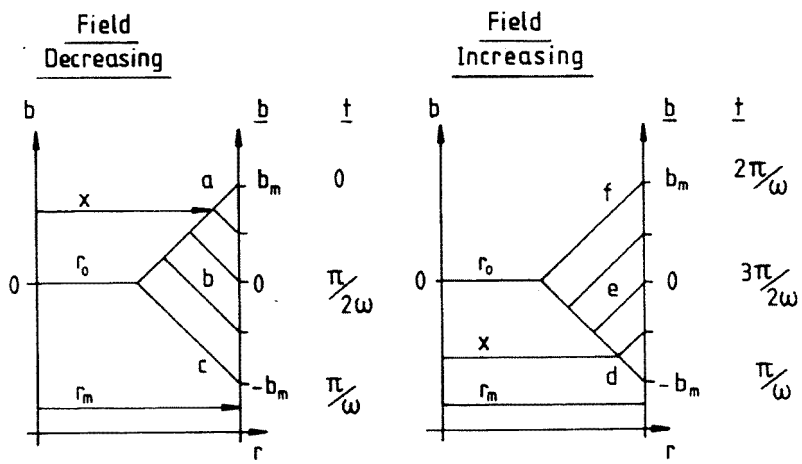

Figure 1. Possible magnetic field profiles inside a superconducting sample as a result of a low a.c. field (a, b, c—field decreasing; d, e, f—field increasing).

2. Theory

2.1. Low a.c. fields

First, a.c. fields less than those required to fully penetrate the sample are considered. In this paper, lower-case letters are used for the a.c. field which in general is smaller than the additional d.c. field. Figure 1 shows the magnetic field profiles which can arise when an a.c. field ($b_A = b_m \cos(\omega t)$) is applied parallel to an infinitely long cylinder (axial $\boldsymbol{b}$) [5]. The magnetic field profiles can be considered in two parts. From a to c, the field decreases from its maximum value, when $b_A = b_m$ at $t = 0$, until the profile is fully reversed, when $b_A = -b_m$ at $t = \pi/\omega$. From d to f, the field increases from its minimum value until the original profile is returned to, at $b_A = +b_m$ and $t = 2\pi/\omega$. It is possible to write

expressions for the magnetic field as a function of radius, $b(r)$, where

$$r_0 \leqslant r < x \qquad b(r) = \pm b_m \mp \left|\frac{\mathrm{d}b(r)}{\mathrm{d}r}\right| (r_m - r) \tag{1}$$

$$x \leqslant r \leqslant r_m \qquad b(r) = +b_A \pm \left|\frac{\mathrm{d}b(r)}{\mathrm{d}r}\right| (r_m - r) \tag{2}$$

where the upper signs are for $0 \leqslant t < \pi/\omega$ and the lower signs for $\pi/\omega \leqslant t < 2\pi/\omega$, r_m is the radius of the sample, $r_m - r_0$ is the maximum distance that the field penetrates into the sample, x is the instantaneous distance at which the gradient in the field profile changes sign, and $|\mathrm{d}b(r)/\mathrm{d}r|$ is equal to $\mu_0 J_c$. From figure 1 it can be seen that

$$x = r_m - \left(\frac{b_m \pm b_A}{2\mu_0 J_c}\right) \tag{3}$$

where the $\pm$ is for increasing/decreasing field. The total flux, ϕ_T, within the sample is obtained by integrating over the cross-sectional area of the sample:

$$\phi_T = \int_0^{r_m} \mathrm{d}\phi. \tag{4}$$

For a cylinder of radius r_m lying parallel to the magnetic field,

$$\phi_T = \int_0^{r_m} 2\pi r b(r)\ \mathrm{d}r. \tag{5}$$

The general equation for the voltage generated across a coil is given by the rate of change of the flux:

$$V(t) = -kL\frac{\mathrm{d}\phi}{\mathrm{d}t} \tag{6}$$

where k is a constant determined by the coil geometry and L is the length of the sample. In flux penetration measurements, the magnetization of the sample is measured using a set of two secondary coils, coils 1 and 2, which are of similar geometry and wound in opposite senses. If the sample is placed in coil 1, the voltage induced across each coil in response to both sections of the a.c. magnetic field can be calculated. In the coil which contains the superconducting sample, equations (1)–(6) are used. In the coil without the superconducting sample, equations (5) and (6) are used where

$$b(r) = b_A.$$

The voltage across coil 1 (with the superconducting sample) is

$$V_1(t) = kL(\pi r_m^2) b_m \omega \left(\left(\frac{b_m}{b_p} - \frac{5b_m^2}{16b_p^2}\right)\sin(\omega t) \mp \left(\frac{b_m}{2b_p} - \frac{b_m^2}{4b_p^2}\right)\sin(2\omega t) + \left(-\frac{b_m^2}{16b_p^2}\right)\sin(3\omega t)\right)$$

where from figure 1, the d.c. field required to fully penetrate the sample is b_p ($b_p = \mu_0 J_c r_m$) and $\mp$ is for decreasing/increasing field. The prefactor ensures that subsequent terms are dimensionless and so can be considered as a differential susceptibility. The voltage across coil 2 (without the superconducting sample) is

$$V_2(t) = kL(\pi r_m^2) b_m \omega \sin(\omega t)$$

for both increasing and decreasing field. The total voltage across both secondary coils is

$$V(t) = V_2(t) - V_1(t).$$

So the total waveform is

$$V(t) = Kb_m\omega[c_1 \sin(\omega t) \pm c_2 \sin(2\omega t) + c_3 \sin(3\omega t)]$$

where the upper signs are for $0 \leqslant t < \pi/\omega$ and the lower signs are for $\pi/\omega \leqslant t < 2\pi/\omega$, and

$$\begin{aligned} K &= kL(\pi r_m^2) \\ c_1 &= \left(1 - \frac{b_m}{b_p} + \frac{5b_m^2}{16b_p^2}\right) \\ c_2 &= \left(\frac{b_m}{2b_p} - \frac{b_m^2}{4b_p^2}\right) \\ c_3 &= \left(\frac{b_m^2}{16b_p^2}\right) \\ b_p &= \mu_0 J_c r_m. \end{aligned} \tag{7}$$

Repeating the analysis for a slab of thickness z and a half-width r_m gives

$$\begin{aligned} K &= kL(2r_m z) \\ c_1 &= \left(1 - \frac{b_m}{2b_p}\right) \\ c_2 &= \left(\frac{b_m}{4b_p}\right) \\ c_3 &= 0 \\ b_p &= \mu_0 J_c r_m. \end{aligned} \tag{8}$$

For a cylinder, of radius r_m, with the field applied perpendicular to the long axis (transverse ***b***), Goldfarb *et al* [6] find that the $c_{1,2,3}$ are twice those for an axial field (using methods outlined by Zenkevitch *et al* [7]). The factor of two accounts for the demagnetization factor in this orientation:

$$\begin{aligned} K &= kL(\pi r_m^2) \\ c_1 &= \left(2 - \frac{2b_m}{b_p} + \frac{5b_m^2}{8b_p^2}\right) \\ c_2 &= \left(\frac{b_m}{b_p} - \frac{b_m^2}{2b_p^2}\right) \\ c_3 &= \left(\frac{b_m^2}{8b_p^2}\right) \\ b_p &= \left(\frac{2}{\pi}\right)\mu_0 J_c r_m. \end{aligned} \tag{9}$$

The total waveform can be expressed as a Fourier series of the form

$$V(t) = Kb_m\omega \sum_{n=1}^{\infty}(a_n \cos(n\omega t) + b_n \sin(n\omega t)) \tag{10}$$

where the dimensionless a_ns and b_ns are given by

$$a_n = \left(\frac{1}{Kb_m\omega}\right)\left(\frac{\omega}{\pi}\right)\int_0^{2\pi/\omega} V(t)\cos(n\omega t)\ \mathrm{d}t$$

and

$$b_n = \left(\frac{1}{K b_m \omega}\right)\left(\frac{\omega}{\pi}\right)\int_0^{2\pi/\omega} V(t)\sin(n\omega t)\ \mathrm{d}t.$$

In the complete solution, the a_ns are

$$a_1 = \left(\frac{8}{3\pi}\right)c_2$$

and

$$a_3 = -\left(\frac{8}{5\pi}\right)c_2$$

and all other odd a_ns are

$$a_n = -\left(\frac{4n}{\pi(n+2)(n-2)}\right)c_2$$

where values of K and $c_{1,2,3}$ are from equations (7)–(9). All even a_ns are zero. The a_ns represent the loss component of the induced voltage, where a_1 is the magnitude of the fundamental frequency. Similarly for the b_ns,

$$b_1 = c_1$$

and

$$b_3 = c_3$$

and all other b_ns are zero. The b_ns represent the lossless component of the induced voltage, where b_1 is the magnitude of the fundamental frequency. These results are consistent with Bean's results for very small a.c. fields [5]. However, the results above are valid over a larger field range, i.e. for all $b_m \leqslant b_p$, and can be used for both cylindrical and slab geometries with appropriate values of $c_{1,2,3}$ and b_p (equations (7)–(9)).

2.2. High a.c. fields ($b_m > b_p$)

The analysis can be extended to a.c. fields greater than those required to fully penetrate the sample. Figure 2 shows the magnetic field profiles which can arise. From a to c, the a.c. field decreases from its maximum value b_m at $t = 0$, until the profile is fully reversed (at $b_A = b_m - 2b_p$ and $t = t_r$) and from c to e, the a.c. field decreases to its minimum value $-b_m$ while the gradient of the field is constant. From e to g, the a.c. field increases from its minimum value until the field profile is fully reversed at $b_A = -b_m + 2b_p$ and $t = \pi/\omega + t_r$ and from g to a, the a.c. field increases to its maximum value and the gradient of the field is constant. As before, it is possible to write expressions for the magnetic field as a function of the radius, i.e. $b(r)$:

$$0 \leqslant r < x \qquad b(r) = \pm b_m \mp \left|\frac{\mathrm{d}b(r)}{\mathrm{d}r}\right|(r_m - r)$$

$$x \leqslant r \leqslant r_m \qquad b(r) = +b_A \pm \left|\frac{\mathrm{d}b(r)}{\mathrm{d}r}\right|(r_m - r)$$

where the upper signs are for $0 \leqslant t < t_r$ and the lower signs for $\pi/\omega \leqslant t < t_r + \pi/\omega$, and

$$0 \leqslant r \leqslant r_m \qquad b(r) = +b_A \pm \left|\frac{\mathrm{d}b(r)}{\mathrm{d}r}\right|(r_m - r)$$

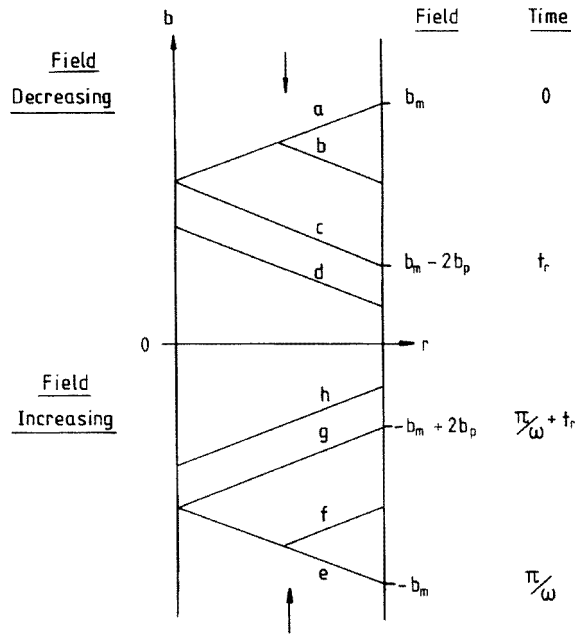

Figure 2. Possible magnetic field profiles inside a superconductor for high a.c. fields. b_p is the field required to fully penetrate the sample and t_r is the time taken to reverse the a.c. field (a → d → e—field decreasing; e → h → a—field increasing).

where the upper signs are for $t_r \leqslant t < \pi/\omega$ and the lower signs for $t_r + \pi/\omega \leqslant t < 2\pi/\omega$ and t_r is the time taken to fully reverse the a.c. field:

$$t_r = \frac{1}{\omega}\cos^{-1}\left[1 - \left(\frac{2\mu_0 J_c r_m}{b_m}\right)\right].$$

The induced voltage is

$$V(t) = K b_m \omega[c_1 \sin(\omega t) \pm c_2 \sin(2\omega t) + c_3 \sin(3\omega t)]$$

where the $c_{1,2,3}$ are given by equations (7)–(9) and the upper signs are for $0 \leqslant t < t_r$ and the lower signs for $\pi/\omega \leqslant t < t_r + \pi/\omega$ and $V(t) = 0$ for all other $t \leqslant 2\pi/\omega$.

Figure 3 shows the induced voltage as a function of time. It is possible to experimentally record such voltage waveforms using a digital storage scope or computerized signal analysis techniques [8–12]. This voltage can also be expressed as a Fourier series in the form of equation (10):

$$V(t) = K b_m \omega \sum_{n=1}^{\infty}(a_n \cos(n\omega t) + b_n \sin(n\omega t)).$$

For the complete solution, the odd a_ns are

$$a_n = \left(\frac{1}{\pi}\right)\left[\sum_{i=1}^{3}\left(\frac{c_i}{n+i}\right)[1 - \cos((n+i)\omega t_r)] - \sum_j \left(\frac{c_j}{n-j}\right)\left[1 - \cos((n-j)\omega t_r)\right]\right].$$

For $n = 1$, $j = 2, 3$; for $n = 3$, $j = 1, 2$; and for $n \geqslant 5$, $j = 1, 2, 3$. All of the even a_ns are zero. The a_ns represent the loss component of the induced voltage. Similarly the odd

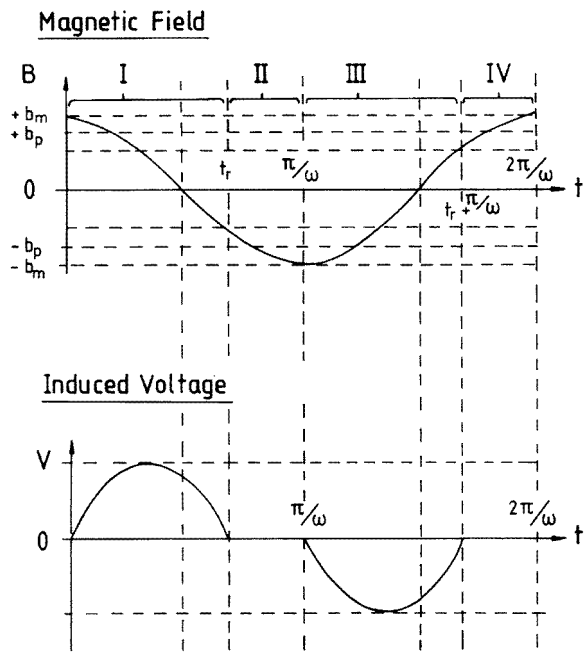

Figure 3. The applied a.c. magnetic field and resulting induced voltage shown as a function of time.

b_ns are

$$b_n = -\left(\frac{1}{\pi}\right)\left[\sum_{i=1}^{3}\left(\frac{c_i}{n+i}\right)\sin((n+i)\omega t_r) - \sum_j\left(\frac{c_j}{n-j}\right)\sin((n-j)\omega t_r) - c_k\omega t_r\right].$$

For $n = 1$, $k = 1$ and $j = 2, 3$; for $n = 3$, $k = 0$ and $j = 1, 2$; and for $n \geqslant 5$, $k = 0$ and $j = 1, 2, 3$. All of the even b_ns are zero. The b_ns represent the lossless component of the induced voltage.

For the loss component, the harmonic voltages measured at the frequency nF ($V_{rms}(nF)$) by the lock-in amplifier (LIA) are simply the time-averaged rms values of $V(t)$, i.e. $\sqrt{1/2}$ times the coefficients of $\cos(n\omega t)$, so $V_{rms}(nF) = \sqrt{1/2}Kb_m\omega a_n$. The lossless voltage lags behind the applied field, since $\sin(\omega t) = \cos(\omega t - \pi/2)$. So for the lossless components, $V_{rms}(nF) = -\sqrt{1/2}Kb_m\omega b_n$. Figures 4 and 5 show the loss and lossless components of the induced voltage for a cylindrical sample in an axial field up to the tenth harmonic. The solutions have been obtained using the mathematical package MATHCAD v6. As before, the equivalent equations for a slab (axial $\boldsymbol{b}$) and cylinder (transverse $\boldsymbol{b}$) can be obtained by substituting the appropriate values for K, $c_{1,2,3}$ and b_p.

For slab and cylindrical geometries, at the fundamental frequency the loss voltage increases as b_m. For all other odd harmonics, the loss voltage first decreases to a minimum and then increases monotonically as b_m (cf. figure 4). For the higher harmonics ($5F$–$9F$), oscillations can be seen in the induced voltage. In contrast, the fundamental and third ($3F$) harmonics of the lossless voltage decrease to a negative value and then increase monotonically to zero as b_m. For all other odd harmonics, the lossless voltage oscillates, then decreases to a negative value before rising to zero as b_m (cf. figure 5). Again, for the higher harmonics ($5F$–$9F$), several oscillations can be seen in the induced voltage.

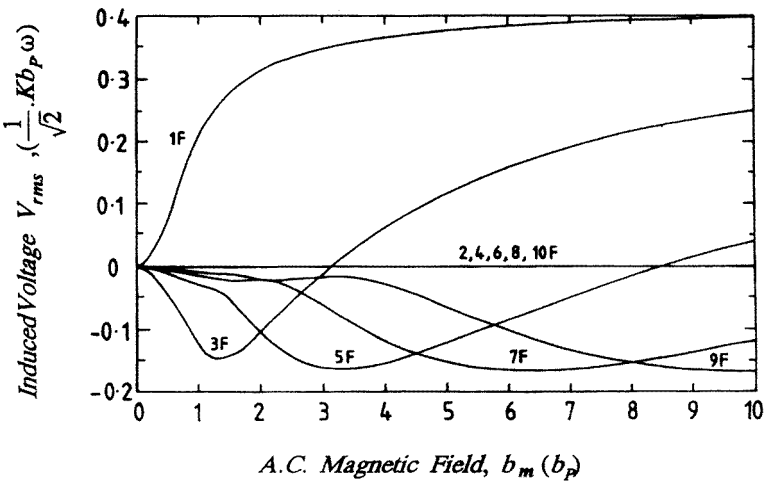

Figure 4. The loss component of the induced harmonic voltage for a cylinder (axial ***b***), where the maximum a.c. field is ten times that required to fully penetrate the sample. Note that all of the even harmonics are zero.

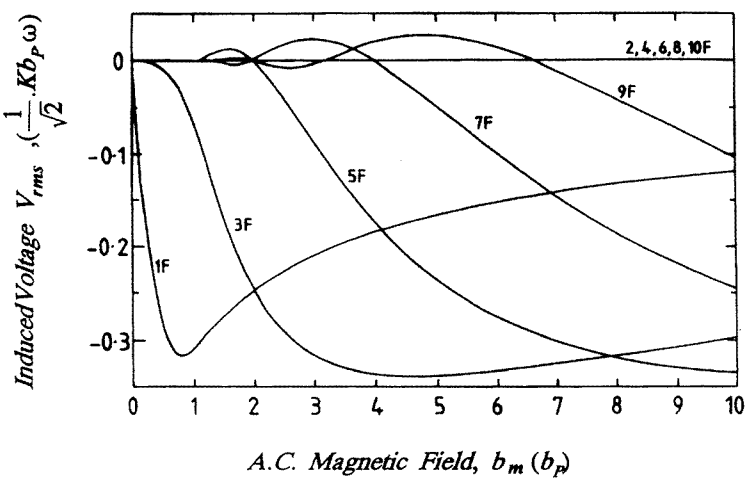

Figure 5. The lossless component of the induced harmonic voltage for a cylinder (axial ***b***), where the maximum a.c. field is ten times that required to fully penetrate the sample. Note that all of the even harmonics are zero.

Oscillations similar to these have been found in a.c. susceptibility measurements [13]. For each of the geometries considered, the minimum value of the lossless voltage is of similar magnitude for all odd harmonics.

For a cylinder, the initial gradient ($\mathrm{d}V_{rms}/\mathrm{d}b_m$) for all odd harmonics of both the loss and lossless induced voltages is twice as large for transverse ***b*** as for axial ***b***, and the field required to fully penetrate the sample (b_p) is a factor of $2/\pi$ lower (cf. equations (7) and (9)). Thus the minimum value of the induced voltage is a factor of $4/\pi \approx 1.27$ higher for transverse ***b*** than for axial ***b***. Table 1 shows the minimum values of the loss and lossless induced voltage (V_{rms}(min)) and the fields at which they occur (b_m(min)) for both

Table 1. Values of V_{rms}(min) and b_{rms}(min) for the loss and lossless induced voltage for both the cylinder and slab samples (axial $\boldsymbol{b}$).

		Loss		Lossless	
Geometry	Harmonic	V_{rms}(min) $((-1/\sqrt{2})Kb_p\omega)$	b_m(min) (b_p)	V_{rms}(min) $((-1/\sqrt{2})Kb_p\omega)$	b_m(min) (b_p)
Cylinder	$1F$	0.00	0.00	0.32	0.80
(axial $\boldsymbol{b}$)	$3F$	0.15	1.35	0.34	4.60
	$5F$	0.16	3.30	0.34	12.39
	$7F$	0.17	6.28	0.34	24.64
	$9F$	0.17	10.25	0.34	39.68
Slab	$1F$	0.00	0.00	0.5	1.00
(axial $\boldsymbol{b}$)	$3F$	0.26	1.75	0.52	6.00
	$5F$	0.28	4.38	0.52	16.22
	$7F$	0.28	8.33	0.52	31.57
	$9F$	0.30	13.62	0.52	52.04

the cylinder and slab (axial $\boldsymbol{b}$). From this table, the minimum value of the lossless induced voltage for the cylinder (axial $\boldsymbol{b}$) at the fundamental frequency ($1F$) is

$$V_{rms}(\text{min}) = -0.32\sqrt{\tfrac{1}{2}}Kb_p\omega. \tag{11}$$

Using equation (6), the probe constant (P) can be written as

$$P = (\mu_0 k\omega)^{-1} = \frac{m_{rms}}{V_{rms}} \tag{12}$$

where V_{rms} is the rms voltage produced by the rms magnetic moment (m_{rms}). Rearranging equations (7), (11) and (12) gives

$$J_c = \frac{\sqrt{2}m_{rms}(\text{min})}{0.32(\pi r_m^2 L)r_m} = 3.125\left(\frac{\sqrt{2}m_{rms}(\text{min})}{V^* r_m}\right) \tag{13}$$

where m_{rms}(min) is the minimum value of the magnetic moment. This result is about 4% higher than the standard d.c. result from the critical-state model, namely $J_c = 3m/V^* r_m$ if $\sqrt{2}m_{rms}$ is substituted for the magnetic moment (m). Similarly for transverse $\boldsymbol{b}$

$$J_c = 3.125\left(\frac{\pi}{4}\right)\left(\frac{\sqrt{2}m_{rms}(\text{min})}{V^* r_m}\right). \tag{14}$$

Using the data in table 1 for the infinite slab,

$$J_c = \frac{\sqrt{2}m_{rms}(\text{min})}{0.5(2Lzr_m)r_m} = \frac{2\sqrt{2}m_{rms}(\text{min})}{V^* r_m} \tag{15}$$

which again is the standard d.c. result for the slab geometry if the same substitution with $\sqrt{2}m_{rms}$ is made. The data in table 1 demonstrate that if the substitution is used for higher harmonics, J_c is accurate to within 4%. If the substitution is used in the standard relation for a rectangular slab, it gives

$$J_c = \frac{2\sqrt{2}m_{rms}(\text{min})}{V^* a_2(1 - a_2/3a_1)}$$

where $2a_1(m)$ and $2a_2(m)$ ($a_1 > a_2$) are the width and the thickness of the samples respectively.

2.3. Magnetic field profiles

The standard magnetic field profile analysis can be completed by differentiating the fundamental harmonic of the lossless voltage with respect to the field, b_m.

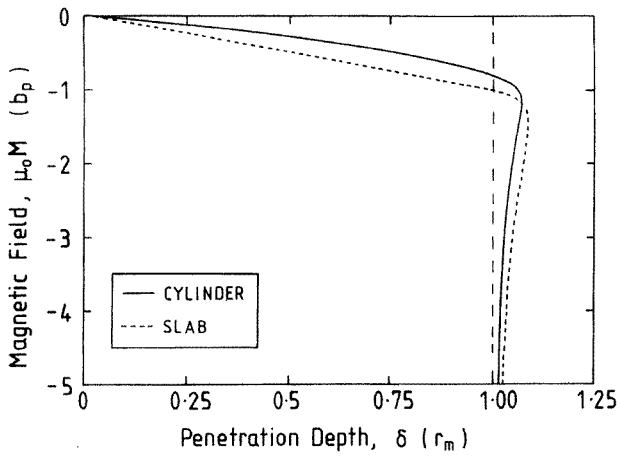

Figure 6. Magnetic field profiles for a slab and a cylinder. δ for the cylinder has been scaled to that of the slab.

For the cylinder (axial $\boldsymbol{b}$), with $b_m < b_p$,

$$V_{rms}(1F) = -\sqrt{\tfrac{1}{2}}Kb_m\omega c_1.$$

Substituting in for c_1 gives

$$V_{rms}(1F) = -\sqrt{\tfrac{1}{2}}Kb_m\omega\left[1 - \frac{b_m}{b_p} + \frac{5b_m^2}{16b_p^2}\right]$$

and differentiating with respect to the a.c. field, b_m,

$$\frac{\mathrm{d}V_{rms}(1F)}{\mathrm{d}b_m} = -\sqrt{\tfrac{1}{2}}K\omega\left[1 - \frac{2b_m}{b_p} + \frac{15b_m^2}{16b_p^2}\right]. \tag{16}$$

This can be rewritten as

$$\frac{|\mathrm{d}V_{rms}(1F)/\mathrm{d}b_m|}{|\mathrm{d}V_{rms}(1F)/\mathrm{d}b_m|_{MAX}} = 1 - 2\left(\frac{\delta}{r_m}\right) + \frac{15}{16}\left(\frac{\delta}{r_m}\right)^2 \tag{17}$$

where the depth that the field penetrates (δ) is

$$\delta = r_m\left(\frac{b_m}{b_p}\right).$$

Solving this quadratic in δ, and taking only the physically meaningful solution, gives

$$\frac{\delta}{r_m} = \frac{16}{15}\left[1 - \left(1 - \frac{15}{16}\left(1 - \frac{|\mathrm{d}V_{rms}(1F)/\mathrm{d}b_m|}{|\mathrm{d}V_{rms}(1F)/\mathrm{d}b_m|_{MAX}}\right)\right)^{1/2}\right].$$

For small a.c. fields, i.e. $b_m \ll b_p$,

$$\delta = \frac{r_m}{2}\left(1 - \frac{|\mathrm{d}V_{rms}(1F)/\mathrm{d}b_m|}{|\mathrm{d}V_{rms}(1F)/\mathrm{d}b_m|_{MAX}}\right) \tag{18}$$

where, from equation (7),

$$r_m = \left(\frac{\sqrt{2}}{kL\pi\omega} \left| \frac{\mathrm{d}V_{rms}(1F)}{\mathrm{d}b_m} \right|_{MAX} \right)^{1/2}.$$

For a cylindrical sample (transverse $\boldsymbol{b}$), equation (18) remains valid, and from equation (8),

$$r_m = \left(\frac{1}{\sqrt{2}kL\pi\omega} \left| \frac{\mathrm{d}V_{rms}(1F)}{\mathrm{d}b_m} \right|_{MAX} \right)^{1/2} \tag{19}$$

but δ has no simple physical interpretation. Repeating the analysis for the slab gives

$$\delta = r_m \left(1 - \frac{|\mathrm{d}V_{rms}(1F)/\mathrm{d}b_m|}{|\mathrm{d}V_{rms}(1F)/\mathrm{d}b_m|_{MAX}} \right) \tag{20}$$

where, from equation (8),

$$r_m = \frac{1}{2kLz\omega} \left| \frac{\mathrm{d}V_{rms}(1F)}{\mathrm{d}b_m} \right|_{MAX}.$$

This analysis can be extended to find the spatial variation of $J_c(\delta)$. For the cylinder (axial $\boldsymbol{b}$), at low a.c. fields, rearranging equations (7), (12) and (16) gives

$$J_c(\delta) = \left| \frac{\sqrt{2}\ \mathrm{d}m_{rms}(\delta)}{(\pi r_m^2)L\ \mathrm{d}\delta} \right| = \frac{1}{V^*} \frac{\sqrt{2}\ \mathrm{d}m_{rms}(\delta)}{\mathrm{d}\delta}$$

where $\mathrm{d}m_{rms}(\delta)/\mathrm{d}\delta$ is the differential of $m_{rms}(\delta)$ with respect to δ. The result is again similar to the standard d.c. result $J_c = \mathrm{d}M(\delta)/\mathrm{d}(\delta)$ as long as $\sqrt{2}m_{rms}$ is substituted for the magnetic moment. In Campbell's original magnetic field profile analysis, where the total flux is measured, the penetration depth is calculated from $\mathrm{d}V/\mathrm{d}b$ (cf. equations (18) and (20)) and the field inside the sample from b. This analysis provides directly the magnetic field profile of the sample. Figure 6 gives the calculated results of a magnetic field profile analysis for a slab and a cylinder (axial $\boldsymbol{b}$), from an analysis at the fundamental frequency. The x-axis (penetration depth, δ) for both geometries is calculated using equation (17) and the y-axis (magnetic field, $\mu_0 M$) is simply b_m. This analysis avoids incorporating non-linear terms and provides a value for δ accurate to a factor of 2. The graph shows the essential features characteristic of a homogeneous sample: the maximum value of the penetration depth δ is approximately equal to the macroscopic dimension of the sample; the gradient in the magnetic field is approximately constant throughout the sample and a region of overshoot in the magnetic field profile is expected. In the original work by Campbell, the total voltage signal was considered and no overshoot found [1].

The magnetic field profile of a granular superconductor can be generated by considering the superposition of two profiles produced by an intra- and intergranular J_c. Figure 7 shows such a magnetic field profile where the characteristic dimension of the grains is a third of that of the sample, but their J_c is a factor of ten higher. For $\delta < r_m$, the figure shows two gradients in the magnetic field, i.e. two values for $\mathrm{d}M/\mathrm{d}\delta$, consistent with two distinct values of J_c. This is a simplified description of a granular system since in practice the outer grains will effectively screen the inner grains. Equally, the two gradients shown in figure 7 cannot be associated with any specific spatial variation in J_c [4]. Nevertheless, figures 6 and 7 show that information can still be obtained about the variation of J_c. In our analysis of a homogeneous sample with a single J_c, a peak is seen at the fundamental frequency of the lossless component of the induced voltage which results in an overshoot in the magnetic field profile. The presence of two distinct gradients and not the overshoot provides evidence for granularity.

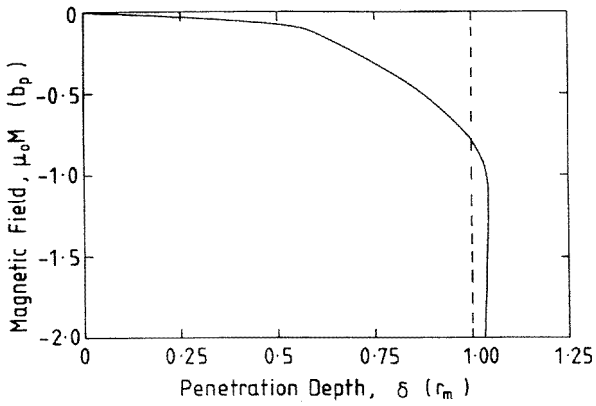

Figure 7. The magnetic field profile for a granular superconductor. The two gradients are a result of the sample having both an inter- and intragranular J_c.

3. Experimental details

3.1. Sample preparation

The sample consisted of a commercial, multifilamentary, superconducting NbTi wire of 61 filaments, each 28 μm in diameter. The copper matrix was removed using nitric acid and the NbTi filaments stuck together with G.E. varnish. 60 sections were cut, each 3 mm long and formed into a sample.

3.2. Experimental procedure

Flux penetration measurements were made from 4.2 K up to T_c in magnetic fields up to 10 T [14, 15]. Measurements are made by applying an increasing a.c. field to a superconducting sample. In agreement with Lenz's law, currents flow to oppose the penetration of the field. Bean's critical-state model shows that the lossless supercurrents flow to a depth δ and are equal to J_c. At intermediate applied a.c. fields, the sample is fully penetrated, i.e. the depth to which the field penetrates (δ) is equal to the radius of the sample (r_m). At this point, a current density equal to J_c flows throughout the entire sample. Eventually high a.c. fields are applied, above those necessary to fully penetrate the sample.

The primary solenoid in these measurements is a two-component oppositely wound a.c. superconducting coil which generates sufficient a.c. field to fully penetrate the sample without quenching the d.c. superconducting magnet [14]. A set of oppositely wound secondary coils were used to measure the magnetization of the sample. At each field, both the loss and lossless components of the induced voltage were recorded for the first ten harmonics with the NbTi filaments perpendicular (transverse $\boldsymbol{b}$) to the a.c. and d.c. field.

3.3. Experimental results

Figure 8 shows the magnetic moment versus a.c. field as a function of temperature for the NbTi sample in a transverse field of 3 T. In this figure, the signal (i.e. the voltage across the secondary coils) has been converted into a magnetic moment using the probe's calibration constant. P was found by calibrating the secondary coils using a Pb sample in the Meissner state. At an operating frequency of 19.7 Hz, $P = 0.277$ A m^2 V^{-1}. The rms

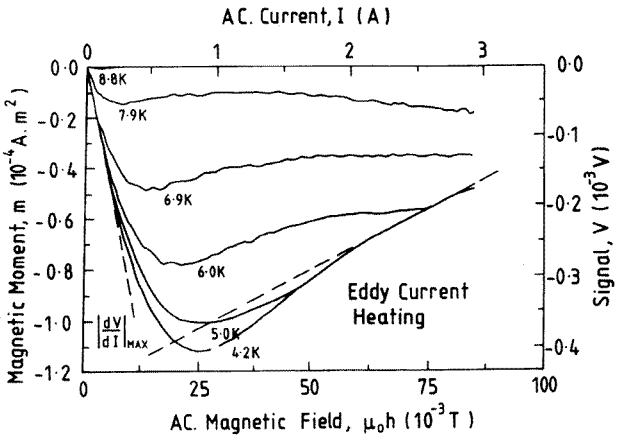

Figure 8. The magnetic moment versus the a.c. field for the NbTi sample as a function of temperature in a transverse field of 3 T.

a.c. current has been converted to a rms a.c. field using the coil constant ($C = 28.7$ mT A^{-1}) which was found using a Hall probe. A background signal, taken when $T > T_c$, has been subtracted from the data. At all temperatures there is a sharp fall in the magnetic moment to a minimum value when there is full penetration of the sample. The marked increase in magnetic moment at the lowest temperatures and highest a.c. fields is attributed to eddy current heating in the copper components of the probe. Other similar measurements on Chevrel phase superconductors confirm the generality of these results [16].

4. Analysis of the results

4.1. Magnetic field profiles

Using the data in figure 8, it is possible to determine magnetic field profiles inside the NbTi sample in terms of P and C. The magnetic field inside the sample ($\mu_0 M$) is

$$\mu_0 M = b_m = C I_{pk}$$

where I_{pk} is the peak value of the current in the primary coil during a cycle. The penetration depth is approximated by

$$\delta = r_m \left(1 - \frac{|\mathrm{d}V_{rms}(1F)/\mathrm{d}I_{rms}|}{|\mathrm{d}V_{rms}(1F)/\mathrm{d}I_{rms}|_{MAX}} \right)$$

where the appropriate value for r_m is found using equations (18), (19) or (20). For the cylinder (transverse $\boldsymbol{b}$) considered here,

$$r_m = \left(\frac{1}{\sqrt{2} k L \pi \omega} \left| \frac{\mathrm{d}V_{rms}(1F)}{\mathrm{d}b_m} \right|_{MAX} \right)^{1/2} = \left(\frac{\mu_0}{2\pi} \frac{P}{nLC} \left| \frac{\mathrm{d}V_{rms}(1F)}{\mathrm{d}I_{rms}} \right|_{MAX} \right)^{1/2}$$

where n is the number of filaments (i.e. $3660 = 60 \times 61$) and $\mathrm{d}V_{rms}(1F)/\mathrm{d}I_{rms}$ is the differential of the signal voltage across the secondary coils with respect to the current in the primary coil. Figure 9 shows the spatial variation in the magnetic field ($\mu_0 M$) as a function of temperature for the sample. The gradient of the lines ($\mathrm{d}M/\mathrm{d}\delta$) as a function of penetration depth gives the spatial variation of J_c.

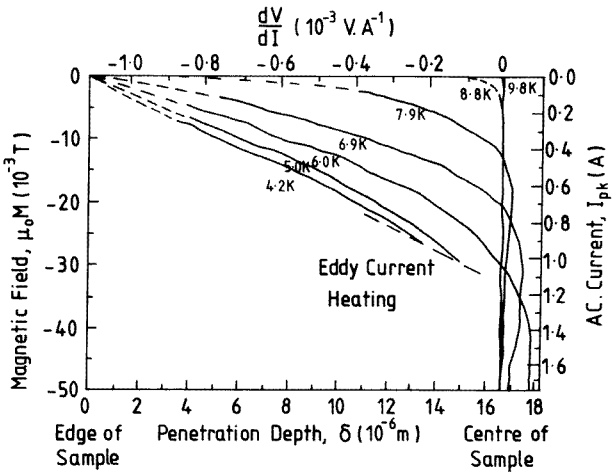

Figure 9. The magnetic field profile inside the NbTi sample as a function of temperature in a transverse field of 3 T.

Only in the case of the axial field orientation can δ be strictly equated to the depth to which the field penetrates, or the magnetization considered as the difference between the applied field and the internal field [17, 18]. However in other geometries, such as the transverse orientation measured here, these quantities can usefully be described by this physical interpretation. In addition, the magnetic measurements of J_c can be directly compared with complementary transport measurements when the sample is in the transverse orientation since there is equivalent current flow in the filaments for both measurements.

It can be seen that the gradient of the lines in figure 9 and hence J_c is approximately constant throughout the sample. This is expected as surface pinning is not a significant mechanism in this wire. The minimum in the magnetic moment (in figure 8) corresponds to an apparent penetration of the magnetic field to a depth greater than the radius of the sample (in figure 9). The fact that this is a artifact of the analysis has been shown in section 2 and is expected even for a bulk pinning superconductor such as NbTi.

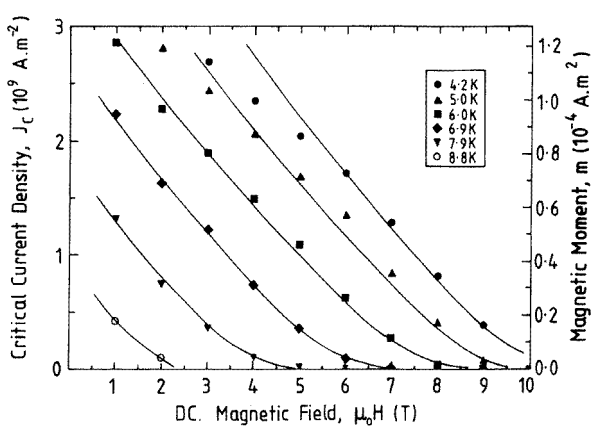

Figure 10. The critical current density of NbTi as a function of field and temperature.

4.2. Critical current density

From the minimum value of the magnetic moment, the coil geometry and the dimensions of the sample, it is possible to calculate the average critical current density at each field and temperature (using equation (14)). This is shown in figure 10. The values of J_c are accurate to about 10%, primarily due to uncertainties in the sample dimensions.

At 6 T and 6 K, J_c is 6.2×10^8 A m^{-2} which is in good agreement with transport current measurements on the same wire that give a value of 6.0×10^8 A m^{-2} [19]. These values of J_c are typical for commercial NbTi wires, although higher values of J_c have been obtained in multifilamentary NbTi by introducing artificial pinning centres to give J_c-values of greater than 1×10^{10} A m^{-2} at 1 T and 4.2 K [20–22].

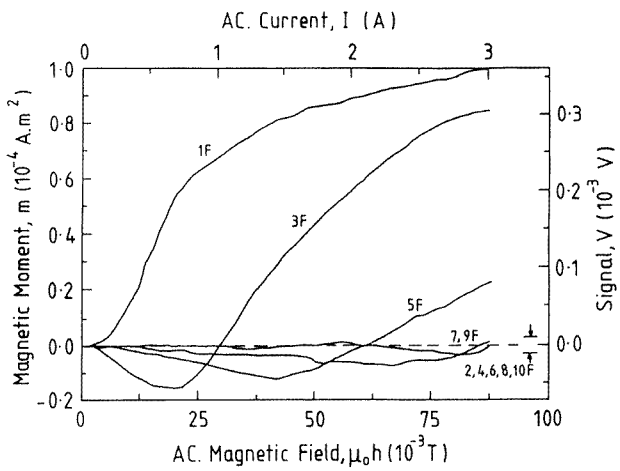

Figure 11. The harmonic response of the loss component of the induced voltage for NbTi at 6 K in a transverse field of 3 T.

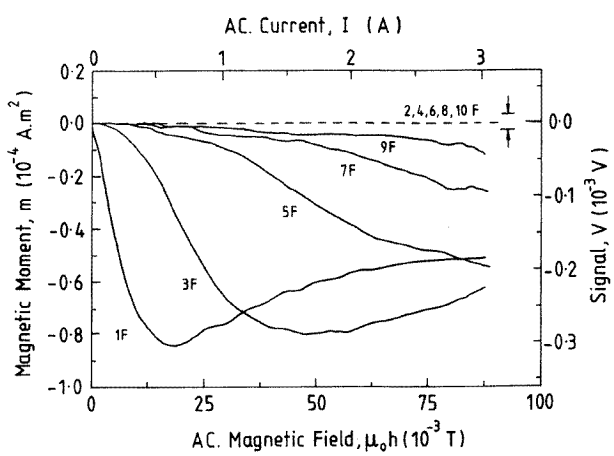

Figure 12. The harmonic response of the lossless component of the induced voltage for NbTi at 6 K in a transverse field of 3 T.

5. Harmonic analysis

Figures 11 and 12 show the harmonic response of both the loss and lossless components of the magnetic moment of NbTi in a transverse field. A background signal, taken when $T > T_c$, has been subtracted from all data. During the experiment a line filter was used to reduce noise and improve the quality of the data. The third ($3F$) harmonic of 19.7 Hz lies close to the line frequency (60 Hz in the USA). The filter both attenuates the signal by a factor of 0.65 and introduces a phase shift of 20°. The $3F$ data have been adjusted to compensate for the filter.

The results are in good agreement with the theoretical predictions in section 2 (cf. figures 4 and 5). All of the even harmonics are zero, i.e. less than $\pm 10\ \mu$V, and the odd harmonics are of the correct sign and functional form. For the loss components (figure 11), there is a factor of 2 in the field at which there is a minimum in the magnetic moment (b_{min}) between $3F$ and $5F$ while the magnitude of the minimum voltages (V_{min}) are similar (consistent with figure 4). For the lossless components (cf. figure 12), there is a factor of 4 in b_{min} between $3F$ and $5F$ and again the magnitudes of these minimum voltages (V_{min}) are similar (consistent with figure 5).

6. Conclusion

A critical-state model has been used to calculate the magnitude and the functional form of the magnetic response of a superconducting sample in an applied a.c. magnetic field. The analysis has been performed for both a cylinder and a slab geometry and evaluated up to the tenth harmonic.

In flux penetration measurements the lossless component of the induced voltage is recorded at the fundamental frequency. Initially, there is a sharp fall in this voltage to a minimum value. Then, the voltage slowly increases as the a.c. field increases beyond that required for full penetration. This result does not depend on the microstructural properties of the sample. This explains that the presence of an overshoot in the magnetic field profile is an artifact of the analysis and cannot be used as direct evidence for granularity. Experimental confirmation of the overshoot in non-granular superconducting materials has been provided.

It is shown that standard expressions derived using the critical-state model relating the current density J_c to the d.c. magnetic moment can be used in a.c. measurements to within an accuracy of 4% by replacing the term for the d.c. magnetic moment by $\sqrt{2}m_{rms}$(min), where m_{rms}(min) is the minimum lossless rms magnetic moment.

Flux penetration measurements have been made on commercial, multifilamentary NbTi, a high-J_c superconductor which exhibits strong bulk pinning. The results have been used to calculate the functional form and spatial variation of J_c as a function of field and temperature. The values of $J_c(B, T)$ are very similar to transport current measurements on the same sample.

The experimental magnetic field profiles and harmonic response of NbTi are consistent with the theoretical analysis for a bulk pinning, homogeneous superconductor.

Acknowledgments

The authors wish to thank P A Russell for help with the production of the figures. This work was supported by the EPSRC, UK, GR/J39588, and the Royal Society, UK.

References

[1] Campbell A M 1969 *J. Phys. C: Solid State Phys.* **2** 1492
[2] Gömöry F, Takács S, Lobotka P, Fröhlich K and Plechácek V 1989 *Physica* C **160** 1
[3] Campbell A M and Blunt F J 1990 *Physica* C **172** 253
[4] Küpfer H, Apfelstedt I, Flükiger R, Keller C, Meier-Hirmer R, Runtsch B, Turowski A, Wiech U and Wolf T 1989 *Cryogenics* **29** 268
[5] Bean C P 1964 *Rev. Mod. Phys.* **36** 31
[6] Goldfarb R, Lelental M and Thompson C 1992 *Magnetic Susceptibility of Superconductors and Other Spin Systems* ed R A Hein *et al* (New York: Plenum) p 49
[7] Zenkevitch V B, Romanyuk A S and Zheltov V V 1980 *Cryogenics* **20** 703
[8] Cave J R 1978 *PhD Thesis* University of Cambridge
[9] Ullamaier H A 1966 *Phys. Status Solidi* **17** 631
[10] Fabbricatore P, Gemme G, Musenich R, Occhetto M and Parodi R 1992 *Cryogenics* **32** 559
[11] Ghatak S K, Mitra A and Sen A 1992 *Phys. Rev.* B **45** 951
[12] Rollins R W and Silcox J 1966 *Solid State Commun.* **4** 323
[13] Ji L, Sohn R H, Spalding G C, Lobb C J and Tinkham M 1989 *Phys. Rev.* B **40** 10 936
[14] Ramsbottom H D and Hampshire D P 1995 *Meas. Sci. Technol.* **6** 1349
[15] Ramsbottom H D and Hampshire D P 1995 *EUCAS'95 (Inst. Phys. Conf. Ser. 148)* (Bristol: Institute of Physics Publishing) p 259
[16] Ramsbottom H D 1996 *PhD Thesis* University of Durham
[17] Campbell A M 1990 *Cryogenics* **30** (S) 809
[18] Campbell A M 1992 *Magnetic Susceptibility of Superconductors and Other Spin Systems* ed R A Hein *et al* (New York: Plenum) p 129
[19] Friend C M and Hampshire D P 1993 *Proc. European Conf. on Applied Superconductivity (Applied Superconductivity 1)* (Oberursel: DGM) p 23
[20] Motowidlo L R, Zeitlin B A, Walker M S and Haldar P 1992 *Appl. Phys. Lett.* **61** 991
[21] Miura O, Inoue I, Suzuki T, Matsumoto K, Tanaka Y, Funaki K, Iwakuma M, Yamafugi K and Matsushita T 1995 *Cryogenics* **35** 169
[22] Miura O, Inoue I, Suzuki T, Matsumoto K, Tanaka Y, Funaki K, Iwakuma M, Yamafugi K and Matsushita T 1995 *Cryogenics* **35** 181